CHINESE OPTICS LETTERS

Vol. 22, No. 2 | February 2024

Inverse-designed Jones matrix metasurfaces for high-performance meta-polarizers

Zhi-Qiang Wang (王志强)[†], Feng-Jun Li (李枫竣)[†], Qian-Mei Deng (邓倩媚), Zhou Wan (万 舟), Xiangping Li (李向平), and Zi-Lan Deng (邓子岚)[*]

Guangdong Provincial Key Laboratory of Optical Fiber Sensing and Communications, Institute of Photonics Technology, Jinan University, Guangzhou 510632, China

[†]These authors contributed equally to this work.

[*]Corresponding author: zilandeng@jnu.edu.cn

Received April 19, 2023 | Accepted October 17, 2023 | Posted Online February 27, 2024

Polarizers have always been an important optical component for optical engineering and have played an indispensable part of polarization imaging systems. Metasurface polarizers provide an excellent platform to achieve miniaturization, high resolution, and low cost of polarization imaging systems. Here, we proposed freeform metasurface polarizers derived by adjoint-based inverse design of a full-Jones matrix with gradient-descent optimization. We designed multiple freeform polarizers with different filtered states of polarization (SOPs), including circular polarizers, elliptical polarizers, and linear polarizers that could cover the full Poincaré sphere. Note that near-unitary polarization dichroism and the ultrahigh polarization extinction ratio (ER) reaching 50 dB were achieved for optimized circular polarizers. The multiple freeform polarizers with filtered polarization state locating at four vertices of an inscribed regular tetrahedron of the Poincaré sphere are designed to form a full-Stokes parameters micropolarizer array. Our work provides a novel approach, we believe, for the design of meta-polarizers that may have potential applications in polarization imaging, polarization detection, and communication.

Keywords: metasurface; inverse design; Jones matrix; polarization imaging.
DOI: 10.3788/COL202422.023601

1. Introduction

Traditional optical imaging systems obtain images by detecting the two-dimensional (2D) spatial light-intensity distribution. Optical polarization imaging provides an additional dimension of polarization information on the basis of traditional intensity imaging, which can not only obtain 2D spatial light-intensity distribution, but also the inherent polarization information for each pixel of the images. When the light wave interacts with the target objects, the inherent geometry, surface roughness, texture, and material would cause a specific polarization responding in the reflected or transmitted light[1]. With the use of polarization information, the physical characteristics of the target objects can be analyzed. In particular, the additional texture and impurity information of the target objects can be effectively detected and identified with full-Stokes polarization imaging. In addition, polarization imaging strategy has exhibited strong antireference capability in complex environments, promising broad application prospects in target detection[2–4], biomedicine[5–7], dehazing imaging[8,9], and atmospheric optics[10].

Unfortunately, conventional polarization imaging systems are always huge and cumbersome, showing limitations that have led to the development of more compact and less cost optical devices[11,12]. Recently, an integrated polarization imaging system has been developed in the division of focal plane (DoFP) framework by integrating micropolarizer array (MPA) with image sensors[13]. The required MPA is typically composed of multiple types of individual micropolarizers that could analyze four basis polarization states. Mostly, the polarization sensing camera could only detect linear polarization components, as the MPAs are only constructed linear micrograting polarizers. Therefore, the advantage of DoFP polarization imaging techniques could not be fully exploited. To achieve the full-Stokes parameters polarization imaging beyond linear polarization detection, high performance MPAs with circular polarizers and even elliptical polarizers are required to form a non-coplanar polarization basis on the Poincaré sphere. Resorting to the forward-designed Jones matrix, MPAs with linear, elliptical, and circular polarizers have been reported[14–17], yet the ER and bandwidth are far from the practical applications for full-Stokes DoFP polarization imaging.

Over the years, the advanced research breakthroughs on metasurfaces have brought great potential to reduce the

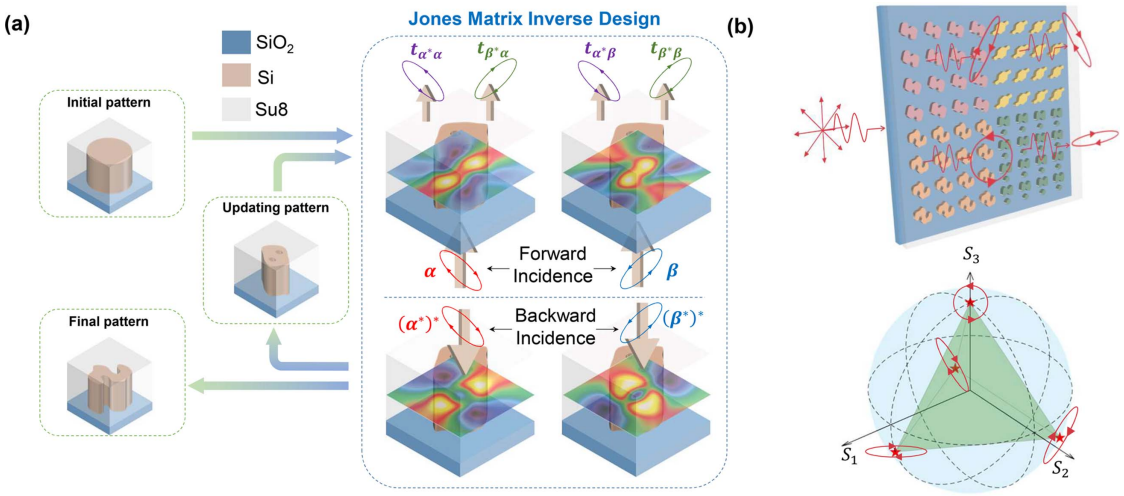

Fig. 1. (a) Schematic of the Jones matrix inverse design algorithm for freeform meta-polarizers optimization; (b) four kinds of freeform polarizers that construct a (top) micropolarizer array and the (bottom) corresponding polarization basis.

limitations of current integrated polarization imaging systems[15,18–23]. Metasurfaces, as an emerging class of multifunctional periodic subwavelength optical elements[24–31], exhibit extremely flexible manipulation of the amplitude[32–34], phase[35–37], and polarization[38–41] of light within a very short light-propagation distance. As the forward design of metasurfaces relies on brute-force parameter sweeps for regular meta-atoms, the final structures are usually not the optimal ones to show the limitations in further improvement of device performance. To design high-performance metasurfaces with an on-demand electromagnetic response, inverse design approaches[42–44] with various optimization algorithms such as heuristic particle swarm, binary search, and genetic algorithms have been studied for years. However, the heuristic inverse design methods are restricted to limited parametric solution space with random testing due to the high computational cost for solving Maxwell's equation. Surprisingly, the inverse design methods based on adjoint-based topology optimization[45–47] provide the spatially varying geometry gradient with only two full-wave simulations at one iteration step, even for very large parametric spaces. Therefore, it provides a convenient and fast algorithm to optimize freeform nanostructures without shape restrictions. Previous adjoint-based inverse design methods were employed to optimize waveguide splitters, metagrating beam deflectors, birefringent metasurfaces, and large-area metalenses, and they have been used to develop many applications of diffraction order management[48–52], structural color[53], polarization control[54], full-space scattering[55], etc., with exceptional performance. However, these works only consider fixed incident polarization states with a one-step optimization. To deal with all possible incident states commonly encountered by a metasurface polarizer, a complete framework for figure of merit (FoM) and spatial gradient calculation in term of a full-Jones matrix with arbitrary polarization basis is highly desired.

In this work, we extend the adjoint-based inverse design approach for full-Jones matrix[56,57] metasurface polarizers with arbitrarily allowed polarization states lying on the Poincaré sphere, which could be particularly used as the MPA device in the polarization imaging system. The Jones matrix metasurfaces with freeform silicon nanoantennas are designed using the adjoint-based inverse design approach with gradient-descent optimization[52]. Throughout the Jones matrix inverse design, the metasurface unit cell pattern is continuously updated along the gradient-descent direction of the pre-set FoM during the iterative evolution process. In each iteration, the spatially varying gradient is precisely calculated by conducting two forward and two adjoint (backward) full-wave simulations with a pair of orthogonal incident polarization states, which are set as the polarizer allowed states and forbidden states, respectively, as schematically shown in Fig. 1(a). Finally, the freeform structure patterns with particular polarization responses are designed. In order to realize full-Stokes DoFP polarization imaging, four types of polarizers, whose analyzed polarization states are located at the vertices of an inscribed regular tetrahedron on the Poincaré sphere, are in high demand. Here, we have successfully designed one circular polarizer and three elliptical polarizers that showed excellent performance with an ultrahigh polarization ER. As shown in Fig. 1(b), the four designed metasurface polarizers can be multiplexed to form a superpixel of MPA. Compared to commercial MPA design, these configuration promises full-Stokes parameter detection with the smallest superpixel size, which shows great application prospects for integrated polarization image sensors.

2. Jones Matrix Inverse Design Framework

In the Jones matrix inverse design for filtering an target input polarization $|\alpha(2\psi, 2\chi)\rangle$, where ψ and χ are azimuth and ellipticity parameters of an arbitrary polarization state located on the Poincaré sphere, one can decompose the incident light on the polarization basis formed by the target polarization and its

orthogonal polarization state ($|\alpha(2\psi, 2\chi)\rangle$, $|\beta(2\psi-\pi, -2\chi)\rangle$). For a planar metasurface, the Jones matrix is constrained as a symmetric matrix; therefore, it is convenient to deal with the output light on the polarization basis constructed by the conjugates of the input polarization basis ($|\alpha^*\rangle$, $|\beta^*\rangle$).

Based on two such polarization bases, we can construct a modified Jones matrix as follows:

$$J^{\#} = \begin{pmatrix} t_{\alpha^*\alpha} & t_{\beta^*\alpha} \\ t_{\alpha^*\beta} & t_{\beta^*\beta} \end{pmatrix}, \tag{1}$$

each element of which represents the complex transmission coefficients of the output polarization state $|o\rangle$ ($o = \alpha^*, \beta^*$) from the incident state $|i\rangle$ ($i = \alpha, \beta$). Assuming the Jones matrix in the linear polarization basis is J, then the elements in modified Jones matrix $J^{\#}$ can be obtained as $t_{\alpha^*\alpha} = \langle\alpha^*|J|\alpha\rangle$, $t_{\beta^*\alpha} = \langle\beta^*|J|\alpha\rangle$, $t_{\alpha^*\beta} = \langle\alpha^*|J|\beta\rangle$, $t_{\beta^*\beta} = \langle\beta^*|J|\beta\rangle$. The target modified Jones matrix for the polarizing incident polarization state $|\alpha\rangle$, while completely blocking its orthogonal state $|\beta\rangle$, will be $J_t^{\#} = \begin{pmatrix} 1 & 0 \\ 0 & 0 \end{pmatrix}$, which corresponds to a Jones matrix in linear polarization basis as $J_t = |\alpha^*\rangle\langle\alpha|$, indicating a polarizer-type functionality that projects arbitrary incident polarizations to state $|\alpha\rangle$ and outputs the $|\alpha^*\rangle$ state. Note that this formula is fundamentally different from the wave-plate-like birefringence metasurface, which must rely on a specified incident polarization state[58]. In the adjoint-based inverse design procedure, we can define four FoMs that correspond to the four matrix elements of the modified Jones matrix, $\mathrm{FoM}_1 = |t_{\alpha^*\alpha}|^2$, $\mathrm{FoM}_2 = |t_{\beta^*\alpha}|^2$, $\mathrm{FoM}_3 = |t_{\alpha^*\beta}|^2$, and $\mathrm{FoM}_4 = |t_{\beta^*\beta}|^2$, and construct the total FoM as follows to meet the target Jones matrix:

$$\mathrm{FoM} = (\mathrm{FoM}_1 - 1)^2 + (\mathrm{FoM}_2 - 0)^2 + (\mathrm{FoM}_3 - 0)^2 + (\mathrm{FoM}_4 - 0)^2. \tag{2}$$

According to the chain rule of differentiation, the gradient of the FoM is

$$\frac{\partial \mathrm{FoM}}{\partial \varepsilon} = 2(\mathrm{FoM}_1 - 1)\frac{\partial \mathrm{FoM}_1}{\partial \varepsilon} + 2\,\mathrm{FoM}_2\frac{\partial \mathrm{FoM}_2}{\partial \varepsilon} + 2\,\mathrm{FoM}_3\frac{\partial \mathrm{FoM}_3}{\partial \varepsilon} + 2\,\mathrm{FoM}_4\frac{\partial \mathrm{FoM}_4}{\partial \varepsilon}, \tag{3}$$

where ε is the spatial distribution of permittivity of the metasurface. Therefore, we should calculate four individual gradients $\frac{\partial \mathrm{FoM}_i}{\partial \varepsilon}$ ($i = 1, 2, 3, 4$) corresponding to the four Jones matrix elements. As shown in Fig. 1(a), the four individual gradients can be calculated by two forward simulations with incident polarization states $|\alpha\rangle$ and $|\beta\rangle$ and two backward simulations with incident polarization states $|(\alpha^*)^*\rangle$ and $|(\beta^*)^*\rangle$. The individual gradients for all four of the Jones matrix elements can be written as[45,52]

$$\frac{\partial \mathrm{FoM}_1}{\partial \varepsilon} = c\,\mathrm{Re}(t^*_{\alpha^*\alpha}\mathbf{E}^{\mathrm{for}}_{\alpha}(\mathbf{r}) \cdot \mathbf{E}^{\mathrm{adj}}_{\alpha}(\mathbf{r})), \tag{4a}$$

$$\frac{\partial \mathrm{FoM}_2}{\partial \varepsilon} = c\,\mathrm{Re}(t^*_{\beta^*\alpha}\mathbf{E}^{\mathrm{for}}_{\alpha}(\mathbf{r}) \cdot \mathbf{E}^{\mathrm{adj}}_{\beta}(\mathbf{r})), \tag{4b}$$

$$\frac{\partial \mathrm{FoM}_3}{\partial \varepsilon} = c\,\mathrm{Re}(t^*_{\alpha^*\beta}\mathbf{E}^{\mathrm{for}}_{\beta}(\mathbf{r}) \cdot \mathbf{E}^{\mathrm{adj}}_{\alpha}(\mathbf{r})), \tag{4c}$$

$$\frac{\partial \mathrm{FoM}_4}{\partial \varepsilon} = c\,\mathrm{Re}(t^*_{\beta^*\beta}\mathbf{E}^{\mathrm{for}}_{\beta}(\mathbf{r}) \cdot \mathbf{E}^{\mathrm{adj}}_{\beta}(\mathbf{r})), \tag{4d}$$

where c is a constant. $\mathbf{E}^{\mathrm{for}}_{\alpha}(\mathbf{r})$ and $\mathbf{E}^{\mathrm{for}}_{\beta}(\mathbf{r})$ are the electric field distribution on one unit-cell of the metasurface on the forward simulations with incident polarization states $|\alpha\rangle$ and $|\beta\rangle$, respectively. $\mathbf{E}^{\mathrm{adj}}_{\alpha}(\mathbf{r})$ and $\mathbf{E}^{\mathrm{adj}}_{\beta}(\mathbf{r})$ are the electric field distribution on the same area of the adjoint (backward) simulations with incident polarization states $|(\alpha^*)^*\rangle = |\alpha\rangle$, $|(\beta^*)^*\rangle = |\beta\rangle$. Substituting Eqs. (4a)–(4d) into Eq. (3), and employing the gradient-descent algorithm, we can update the unit-cell meta-atoms from an achiral pattern to planar chiral patterns with an ultrahigh polarization ER and predesigned ellipticity. In our design, which we base on an adjoint topology optimization method[52], the blur function is used to remove the small dielectric features in the iterative process. The contrast function is also applied to gradually push the blurring dielectric pattern toward the binary pattern during the optimization. In the following, we will employ such an inverse design method to design a variety of freeform metasurface polarizers that could filter specific arbitrary polarization state on the Poincaré sphere.

3. Structure Optimization Results

Figure 2 shows the iterative evolution of the freeform metasurface circular polarizer and its optical performance. The chosen target polarization state is the right-handed circular polarization (RHCP) state $|\alpha(\psi_0 = 0°, \chi_0 = 45°)\rangle$, as shown in Fig. 2(a).

In order to determine the best initial parameters, the preoptimization is used by roughly optimizing several possible values of height, diameter, and period of unit-cell. After that, the initial design consists of a silicon nanocylinder array with a height of 500 nm, a diameter of 360 nm, and a periodicity of 600 nm on a fused silica substrate. In addition, an 850 nm thick photoresist superstrate is considered to protect the nanostructures. We apply both two forward and two backward full-wave simulations in each iterative optimization. In Fig. 2(b), the transmission coefficients of the four Jones matrix components are calculated in each iteration step. In this case, the transmission coefficients of the four Jones matrix components are calculated by placing a source at the silicon substrate and a monitor above the photoresist superstrate. In addition, the reflection loss at the photoresist–air boundary and air–substrate boundary has already been considered in our inverse design model. During the optimization, only the T_{LR} component clamps up to 1, and the other three components finally drop to 0 during the optimization. This indicates that RHCP light perfectly passes through the optimized circular polarizer while the orthogonal state is blocked, which is in great agreement with the target

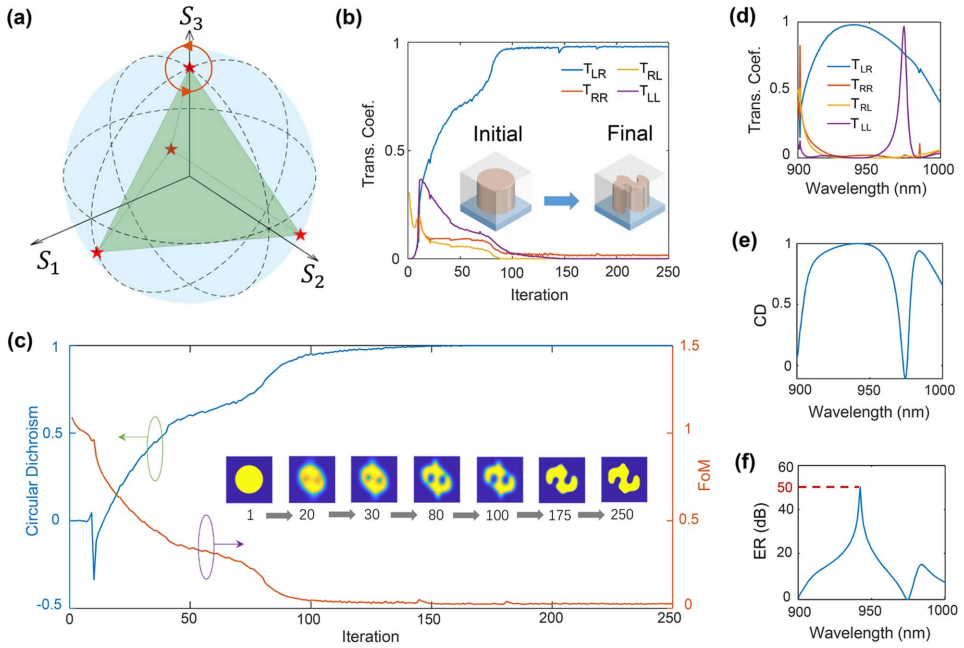

Fig. 2. (a) Schematic of the Poincaré sphere location of the target RCP state at the North Pole; (b) iterative evolution process of the four Jones matrix elements for the circular polarizer; inset, diagrams for the initial structure and the evolved final structure; (c) iterative evolution process of the CD and the FoM; inset, iterative evolution of the freeform structure; (d)–(f) transmission spectra of (d) all Jones matrix elements, (e) CD spectrum and (f) ER spectrum of the optimized freeform pattern. The structure parameters of the initial pattern are a period of 600 nm, a height of 500 nm, and a diameter of 360 nm.

Jones matrix. To further characterize the performance of the optimized polarizer, we define the polarization dichroism (PD) and ER as

$$\mathrm{PD} = \frac{|t_{\alpha^*\alpha}|^2 + |t_{\beta^*\alpha}|^2 - |t_{\alpha^*\beta}|^2 - |t_{\beta^*\beta}|^2}{|t_{\alpha^*\alpha}|^2 + |t_{\beta^*\alpha}|^2 + |t_{\alpha^*\beta}|^2 + |t_{\beta^*\beta}|^2}, \tag{5}$$

$$\mathrm{ER} = \frac{|t_{\alpha^*\alpha}|^2 + |t_{\beta^*\alpha}|^2}{|t_{\alpha^*\beta}|^2 + |t_{\beta^*\beta}|^2}. \tag{6}$$

For the circular polarizer case, the PD is equivalent to the circular dichroism (CD) possessed by the planar chiral pattern. In Fig. 2(c), we plot the CD and the FoM over the course of the optimization process for the circular metasurface polarizer. Over the iteration, the CD increases from zero to a near-unitary value, and the FoM continuously declines and finally converges to a minimum. When the number of iteration steps is close to 10 in Fig. 2(c), the CD drops sharply and then rises again. The reason for this phenomenon should be that the iteratively optimized structure is unstable when the structure changes rapidly in the beginning period of the iteration process. In the following steps, the CD actually always shows some oscillations, yet the strength is not that strong, and in the last steps (200–250), the CD becomes stable and converges to the highest value, 1. The inset in Fig. 2(c) also proved that our Jones matrix inverse design algorithm can be used to optimize the nonspecific polarization responding device to possess a strong planar chirality. Figures 2(d)–2(f) show the detailed performance of the designed circular polarizer within the wavelength from 900 to 1000 nm, which is in good agreement with the optimization results. The CD is above 0.9, within wavelength range from 915 to 960 nm, and reaches near-unity at the target wavelength, 940 nm. Importantly, the maximum ER reaches as high as 50 dB, which is a remarkable improvement over previous work based on forward design[15,59–62], as shown in Table 1.

In order to clarify the optical modes supported by the high-performance freeform circular polarizer, the electric, magnetic field distribution, and multipole decomposition spectra are calculated, as shown in Fig. S1 (Supplementary Material). The special intensity profile shows a chiral distribution. Mode expansion calculations show that the toroidal dipole (TD), the electric dipole (ED), and the magnetic dipole (MD) are the main contributing multipoles for the scattering properties. The chiral response is attributed to multiple mode interferences, in which

Table 1. Comparison of the Circular Polarizers with the Reported Studies on Theoretical Circular Polarization ERs.

Work	Theoretical Circular Polarization ER
Wegener *et al.*[59]	9 dB
Yao *et al.*[60]	16 dB
Wang *et al.*[61]	14 dB
Ozbay *et al.*[62]	23 dB
This work	**50 dB**

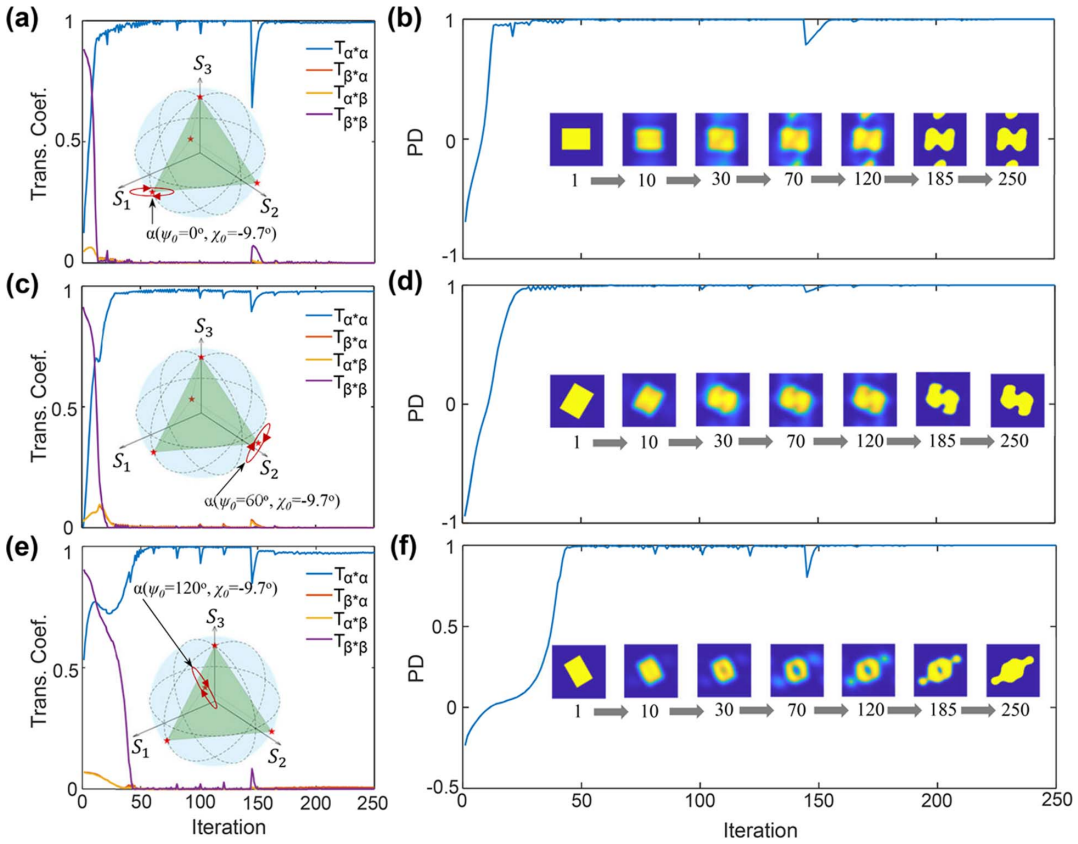

Fig. 3. (a), (c), (e) Iterative evolution process of the four Jones matrix elements and (b), (d), (f) polarization dichroism of the metasurface-based elliptical polarizer at three locations of the Poincaré sphere. (a), (b) $\psi_0 = 0°$, $\chi_0 = -9.7°$; (c), (d) $\psi_0 = 60°$, $\chi_0 = -9.7°$; and (e), (f) $\psi_0 = 120°$, $\chi_0 = -9.7°$. The structure parameters of the initial patterns are a period of 600 nm, a height of 500 nm; the length and width of the three elliptical polarizers are 310 nm × 230 nm, 330 nm × 250 nm, and 300 nm × 210 nm, respectively.

the magnitude of the TD is the highest, while the contributions of other modes are nonnegligible.

In addition to the circular polarizer, we then optimize three freeform elliptical polarizers located at the other three vertices of the inscribed regular tetrahedron on the Poincaré sphere (by setting the target polarization parameters as $\psi_0 = 0°$, $\chi_0 = -9.7°$; $\psi_0 = 60°$, $\chi_0 = -9.7°$, and $\psi_0 = 120°$, $\chi_0 = -9.7°$), as shown in Fig. 3. In the early stage of the iteration process, the transmission coefficient and PD of the target polarization state rapidly approach unity and then stay steady, showing relatively fast convergent speed of our purposed algorithm. The insets of Figs. 3(b), 3(d), and 3(f) show the evolution of the 2D patterns of all three elliptical polarizers at several iteration steps. To optimize the elliptical polarizers, the initial patterns are selected as rectangular nanoblocks whose orientation angles are set to be equal to the azimuth parameter ψ of the target polarization states. In this way, the nanoblocks can capture the anisotropic polarization response to quickly converge to a local optimum for the target elliptical polarization. Importantly, our proposed Jones matrix inverse design strategy is readily combined with global optimization algorithms such as particle swarm optimization (PSO) or artificial neural network by properly adjusting the target function or loss function. Moreover, as we pixelated the structure patterns with a continuously varying permittivity profile, although the pattern variations are very small in the later stage of the iterative optimization, they are still not binarized. Therefore, enough steps of iteration are needed to obtain the practical binarized patterns, although the PD values are almost unchanged from 50 to 250 iteration steps. As the C4 symmetry of the square lattice, which is not in line with the C3 cylindrical symmetry of the three elliptical polarizations, the finally optimized patterns are not cylindrically symmetric. This noncylindrical symmetry of final patterns may also be attributed to the need for a strong anisotropic response for target elliptical polarization of dielectric structures.

Figure 4 shows the optimized metasurface unit-cell patterns and performance spectra in a relatively wide band (900–1000 nm) of the three optimized elliptical polarizers. The transmission spectra of all the four Jones matrix components ($T_{\alpha^*\alpha} = |t_{\alpha^*\alpha}|^2$, $T_{\beta^*\alpha} = |t_{\beta^*\alpha}|^2$, $T_{\alpha^*\beta} = |t_{\alpha^*\beta}|^2$, and $T_{\beta^*\beta} = |t_{\beta^*\beta}|^2$) exhibit the best performance near the target wavelength of 940 nm, with $T_{\alpha^*\alpha} = 1$, and the other three elements $T_{\beta^*\alpha} = T_{\alpha^*\beta} = T_{\beta^*\beta} = 0$, which are consistent with the polarizer-like target Jones matrix $J^{\#}$. Note that the highly efficient performance is not sensitive to the wavelength, which is sustained in a flat-top bandwidth even though we have not used the multiwavelength optimization yet, as shown in Figs. 4(b), 4(f), and 4(j). Especially

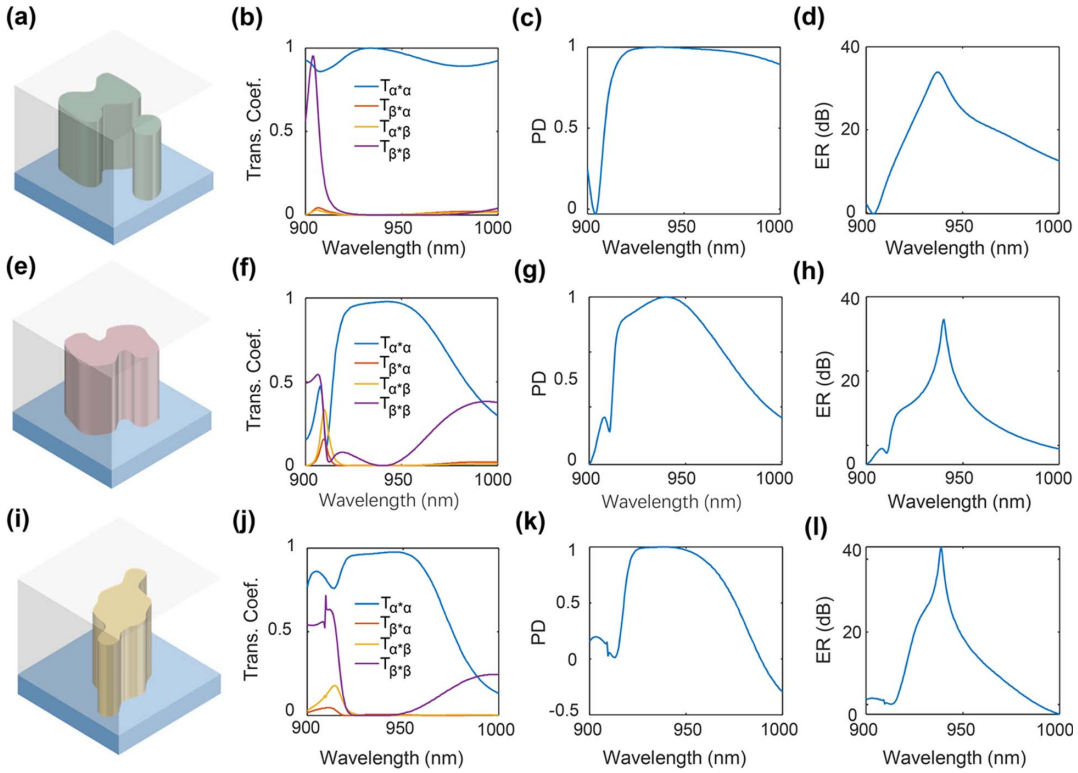

Fig. 4. (a), (e), (i) Schematic of the finally optimized meta-atom structure; (b), (f), (j) transmission spectra in terms of all Jones matrix elements; (c), (g), (k) polarization dichroism spectrum and ER spectrum; (d), (h), (i) of the freeform elliptical polarizer for polarization parameters. (a)–(d) $\psi_0 = 0°$, $\chi_0 = -9.7°$; (e)–(h) $\psi_0 = 60°$, $\chi_0 = -9.7°$; (i)–(l) $\psi_0 = 120°$, $\chi_0 = -9.7°$.

in the elliptical polarizer with allowed polarization parameters $\psi_0 = 0°$ and $\chi_0 = -9.7°$, a broadband characteristic is exhibited and the polarization dichroism remains above 0.9 in the wavelength range from 915 to 1000 nm. In Figs. 4(c), 4(g), and 4(k), the PD spectra show the near-unitary peak at the target wavelength, and the ER spectra reach 30 dB for all three elliptical freeform polarizers. As the simulation results have shown, the optimized freeform metasurface polarizers promise a convenient design for full-Stokes parameters MPA as well as huge potential in compact polarization imaging systems.

For full-Stokes parameter polarization imaging applications, the polarization measurement basis could be chosen in many ways, as long as their coordinates lie at the vertices of the regular polyhedron inscribed in the Poincaré sphere. To demonstrate the flexibility of the measurement framework, we have also designed another set of MPAs that include two elliptical polarizers and two linear polarizers with allowed polarization parameters (1) $\psi_0 = 0°$, $\chi_0 = 27.4°$; (2) $\psi_0 = 0°$, $\chi_0 = -27.4°$; (3) $\psi_0 = 62.6°$, $\chi_0 = 0°$; and (4) $\psi_0 = 117.4°$, $\chi_0 = 0°$, as shown in insets of Figs. S3(a, c, e, g) (Supplementary Material). Figures S3(b, d, f, h) (Supplementary Material) show the PD and structure pattern evolution process for the four target polarizers. The initial structures of the polarizers are set as rectangular patterns, whose orientation angles are equal to the azimuth parameter ψ of the target polarizer. From the performance spectra shown in Fig. S4 (Supplementary Material), surprisingly, it could be found that all the linear and elliptical polarizers have a broader bandwidth than the former MPA design. Further, we also optimized all the freeform polarizers demonstrated above at strong asymmetric index environment consisting of a silicon dioxide substrate and an air superstrate. Again, the excellent performance in terms of transmission efficiency, PD, and ER can be maintained as shown in Figs. S5–S8 (Supplementary Material), but with totally different freeform shapes. For our designed polarizers, it seems that the index environment asymmetry would benefit in strong bianisotropic freeform structure optimization. The better performance would be achieved by the suitable choice of measurement polarization framework and the asymmetric index environment. The range of structural parameters of the polarizer we designed meets the conditions that can be achieved by current nanofabrication technology, and can be processed and manufactured by electron beam lithography (EBL). It mainly goes through the processes of substrate surface pretreatment, deposition, patterning, lift-off, and etching. In the deposition process, 500 nm-thick amorphous silicon (α-Si) is used. And, taking the circular polarizer as an example, we also performed structural error analysis in Fig. S11 (Supplementary Material).

The above Jones matrix inverse design procedure is computed with a single-target wavelength, and thus cannot achieve the broadband optimization for an arbitrary given polarization. Therefore, the multiwavelength inverse design method could be employed to design the broadband freeform polarizers. In order to provide larger parameter space for optimizing

broadband polarizers, a diatomic initial structure is chosen for multiwavelength Jones matrix optimization. Figure S9 (Supplementary Material) shows a comparison of the bandwidth performance between a monoatomic single-wavelength elliptical polarizer ($\psi_0 = 0°$, $\chi_0 = 27.4°$) and a diatomic multiwavelength elliptical polarizer ($\psi_0 = 0°$, $\chi_0 = 27.4°$). For the monoatomic single-wavelength optimization [Figs. S9(a)–S9(d) in Supplementary Material], the transmission spectra of the finally optimized freeform structure only perform well at a narrow bandwidth, around the target wavelength of 1000 nm [Fig. S9(d) in Supplementary Material], while for the diatomic three-wavelength optimization [Figs. S9(e)–S9(h) in Supplementary Material], the FoM at multiple target wavelengths 850, 950, and 1000 nm simultaneously evolves toward the minima, and the PDs reach above 0.9. The diatomic design approach is chosen here, as it has a larger degree of design freedom than the monoatomic design. The transmission spectra of the optimized diatomic freeform metasurface shown in Fig. S9(h) (Supplementary Material) manifest a flat-top broadband property from 850 to 1000 nm. Moreover, our proposed multiwavelength Jones matrix optimizer can readily extend to more complex objective optimization wavelengths for different polarization bases, as shown in Fig. S10 (Supplementary Material). Compared with the single-wavelength optimization, the bandwidth of the polarizer can be significantly expanded when we applied more target wavelength to the optimizer. Although the transmission spectra exhibit sharp dips over the broad bandwidth, which mainly may be attributed to the poor convergence of designed algorithm for large parameterization space, it still provides a feasible pathway for broadband polarizer optimization.

4. Conclusions

To conclude, we have proposed inverse designed Jones matrix metasurface polarizers that could filter arbitrary polarization states on the Poincaré sphere with high efficiency and an ER beyond the previous multiplexing metasurface. Four kinds of polarizers with filtered polarizations located on the four vertices of a regular tetrahedron form a complete polarization measurement basis for full-Stokes parameter polarization imaging. The extended adjoint-based full-Jones matrix inverse design algorithm provides an efficient way to optimize the desired freeform structure that converts unpolarized incident light into a specific polarized light state with unitary PD and an extremely high ER, reaching 50 dB. Further, the Jones matrix inverse design algorithm could be further implemented with multiwavelength and multi-atom configurations to enlarge the parameterization space for improving the bandwidth of the metasurface. In addition, the designed freeform polarizers can be readily arranged as an MPA, which can be integrated with CCD or CMOS to form a full polarization sensor for a compact polarization imaging system, promoting great application prospects in computational high-dimension imaging, defect detection, and atmospheric exploration.

Acknowledgements

This work was supported by the National Key Research and Development Program of China (Nos. 2022YFB3607300 and 2021YFB2802003), the National Natural Science Foundation of China (NSFC) (No. 62075084), and the Guangdong Basic and Applied Basic Research Foundation (No. 2022B1515020004).

References

1. J. R. Schott, *Fundamentals of Polarimetric Remote Sensing* (SPIE Press, 2009).
2. G. Luc, F. Alban, and B. Laurent, "Full Stokes polarimetric imaging using a single ferroelectric liquid crystal device," Opt. Eng. **50**, 081209 (2011).
3. J. Guan and J. Zhu, "Target detection in turbid medium using polarization-based range-gated technology," Opt. Express **21**, 14152 (2013).
4. N. Vannier, F. Goudail, C. Plassart, *et al.*, "Comparison of different active polarimetric imaging modes for target detection in outdoor environment," Appl. Opt. **55**, 2881 (2016).
5. J. Wang, W. Zheng, K. Lin, *et al.*, "Integrated Mueller-matrix near-infrared imaging and point-wise spectroscopy improves colonic cancer detection," Biomed. Opt. Express **7**, 1116 (2016).
6. A. Sanaz and I. A. Vitkin, "Polarized light imaging in biomedicine: emerging Mueller matrix methodologies for bulk tissue assessment," J. Biomed. Opt. **20**, 061104 (2015).
7. P. Tang, M. A. Kirby, N. Le, *et al.*, "Polarization sensitive optical coherence tomography with single input for imaging depth-resolved collagen organizations," Light Sci. Appl. **10**, 237 (2021).
8. E. Namer, S. Shwartz, and Y. Y. Schechner, "Skyless polarimetric calibration and visibility enhancement," Opt. Express **17**, 472 (2009).
9. J. Liang, W. Zhang, L. Ren, *et al.*, "Polarimetric dehazing method for visibility improvement based on visible and infrared image fusion," Appl. Opt. **55**, 8221 (2016).
10. W. Zhang, X. Zhang, Y. Cao, *et al.*, "Robust sky light polarization detection with an S-wave plate in a light field camera," Appl. Opt. **55**, 3518 (2016).
11. J. S. Tyo, D. L. Goldstein, D. B. Chenault, *et al.*, "Review of passive imaging polarimetry for remote sensing applications," Appl. Opt. **45**, 5453 (2006).
12. Z. Wu, P. E. Powers, A. M. Sarangan, *et al.*, "Optical characterization of wire-grid micropolarizers designed for infrared imaging polarimetry," Opt. Lett. **33**, 1653 (2008).
13. R. David, R. Maik, and N. Gunther, "Principle investigations on polarization image sensors," Proc. SPIE **11144**, 111440A (2019).
14. K. A. Bachman, J. J. Peltzer, P. D. Flammer, *et al.*, "Spiral plasmonic nano-antennas as circular polarization transmission filters," Opt. Express **20**, 1308 (2012).
15. C. Zhang, J. Hu, Y. Dong, *et al.*, "High efficiency all-dielectric pixelated metasurface for near-infrared full-Stokes polarization detection," Photonics Res. **9**, 583 (2021).
16. S. Wang, Z.-L. Deng, Y. Wang, *et al.*, "Arbitrary polarization conversion dichroism metasurfaces for all-in-one full Poincaré sphere polarizers," Light Sci. Appl. **10**, 24 (2021).
17. S. Wang, S. Wen, Z.-L. Deng, *et al.*, "Metasurface-based solid Poincaré sphere polarizer," Phys. Rev. Lett. **130**, 123801 (2023).
18. N. A. Rubin, G. D'Aversa, P. Chevalier, *et al.*, "Matrix Fourier optics enables a compact full-Stokes polarization camera," Science **365**, eaax1839 (2019).
19. Y. Zhang, M. Pu, J. Jin, *et al.*, "Crosstalk-free achromatic full Stokes imaging polarimetry metasurface enabled by polarization-dependent phase optimization," Opto-Electron. Adv. **5**, 220058 (2022).
20. Z. Yang, Z. Wang, Y. Wang, *et al.*, "Generalized Hartmann-Shack array of dielectric metalens sub-arrays for polarimetric beam profiling," Nat. Commun. **9**, 4607 (2018).
21. C. Yan, X. Li, M. Pu, *et al.*, "Midinfrared real-time polarization imaging with all-dielectric metasurfaces," Appl. Phys. Lett. **114**, 161904 (2019).
22. Y. Ren, S. Guo, W. Zhu, *et al.*, "Full-Stokes polarimetry for visible light enabled by an all-dielectric metasurface," Adv. Photonics Res. **3**, 2100373 (2022).
23. E. Arbabi, S. M. Kamali, A. Arbabi, *et al.*, "Full-Stokes imaging polarimetry using dielectric metasurfaces," ACS Photonics **5**, 3132 (2018).

24. N. Yu, P. Genevet, M. A. Kats, *et al.*, "Light propagation with phase discontinuities: generalized laws of reflection and refraction," Science **334**, 333 (2011).
25. S. Sun, Q. He, S. Xiao, *et al.*, "Gradient-index meta-surfaces as a bridge linking propagating waves and surface waves," Nat. Mater. **11**, 426 (2012).
26. J. Li, G. Hu, L. Shi, *et al.*, "Full-color enhanced second harmonic generation using rainbow trapping in ultrathin hyperbolic metamaterials," Nat. Commun. **12**, 6425 (2021).
27. X. Yin, H. Zhu, H. Guo, *et al.*, "Hyperbolic metamaterial devices for wavefront manipulation," Laser Photonics Rev. **13**, 1800081 (2019).
28. Z. Ju, J. Wen, L. Shi, *et al.*, "Ultra-broadband high-efficiency airy optical beams generated with all-silicon metasurfaces," Adv. Opt. Mater. **9**, 2001284 (2021).
29. S. So, J. Mun, J. Park, *et al.*, "Revisiting the design strategies for metasurfaces: fundamental physics, optimization, and beyond," Adv. Mater. **35**, 2206399 (2022).
30. Y. Yang, J. Seong, M. Choi, *et al.*, "Integrated metasurfaces for re-envisioning a near-future disruptive optical platform," Light Sci. Appl. **12**, 152 (2023).
31. Z. Feng, T. Shi, G. Geng, *et al.*, "Dual-band polarized upconversion photoluminescence enhanced by resonant dielectric metasurfaces," eLight **3**, 21 (2023).
32. Q. Fan, M. Liu, C. Zhang, *et al.*, "Independent amplitude control of arbitrary orthogonal states of polarization via dielectric metasurfaces," Phys. Rev. Lett. **125**, 267402 (2020).
33. G.-Y. Lee, G. Yoon, S.-Y. Lee, *et al.*, "Complete amplitude and phase control of light using broadband holographic metasurfaces," Nanoscale **10**, 4237 (2018).
34. M. Liu, W. Zhu, P. Huo, *et al.*, "Multifunctional metasurfaces enabled by simultaneous and independent control of phase and amplitude for orthogonal polarization states," Light Sci. Appl. **10**, 107 (2021).
35. R. Zhao, B. Sain, Q. Wei, *et al.*, "Multichannel vectorial holographic display and encryption," Light Sci. Appl. **7**, 95 (2018).
36. G. Zheng, H. Mühlenbernd, M. Kenney, *et al.*, "Metasurface holograms reaching 80% efficiency," Nat. Nanotechnol. **10**, 308 (2015).
37. L. Wang, S. Kruk, H. Tang, *et al.*, "Grayscale transparent metasurface holograms," Optica **3**, 1504 (2016).
38. Z.-L. Deng, J. Deng, X. Zhuang, *et al.*, "Diatomic metasurface for vectorial holography," Nano Lett. **18**, 2885 (2018).
39. Z.-L. Deng, M. Jin, X. Ye, *et al.*, "Full-color complex-amplitude vectorial holograms based on multi-freedom metasurfaces," Adv. Funct. Mater. **30**, 1910610 (2020).
40. K. Huang, H. Liu, F. J. Garcia-Vidal, *et al.*, "Ultrahigh-capacity non-periodic photon sieves operating in visible light," Nat. Commun. **6**, 7059 (2015).
41. J. Kim, Y. Yang, T. Badloe, *et al.*, "Geometric and physical configurations of meta-atoms for advanced metasurface holography," InfoMat **3**, 739 (2021).
42. S. So, J. Kim, T. Badloe, *et al.*, "Multicolor and 3D holography generated by inverse-designed single-cell metasurfaces," Adv. Mater. **35**, 2208520 (2023).
43. S. So, T. Badloe, J. Noh, *et al.*, "Deep learning enabled inverse design in nanophotonics," Nanophotonics **9**, 1041 (2020).
44. Z. Li, R. Pestourie, J.-S. Park, *et al.*, "Inverse design enables large-scale high-performance meta-optics reshaping virtual reality," Nat. Commun. **13**, 2409 (2022).
45. C. M. Lalau-Keraly, S. Bhargava, O. D. Miller, *et al.*, "Adjoint shape optimization applied to electromagnetic design," Opt. Express **21**, 21693 (2013).
46. S. Molesky, Z. Lin, A. Y. Piggott, *et al.*, "Inverse design in nanophotonics," Nat. Photonics **12**, 659 (2018).
47. M. Zhou, D. Liu, S. W. Belling, *et al.*, "Inverse design of metasurfaces based on coupled-mode theory and adjoint optimization," ACS Photonics **8**, 2265 (2021).
48. Z. Wang, C. Dai, Z. Li, *et al.*, "Free-space optical merging via meta-grating inverse-design," Nano Lett. **22**, 2059 (2022).
49. H. Chung and O. D. Miller, "Tunable metasurface inverse design for 80% switching efficiencies and 144° angular deflection," ACS Photonics **7**, 2236 (2020).
50. P. Thureja, G. K. Shirmanesh, K. T. Fountaine, *et al.*, "Array-level inverse design of beam steering active metasurfaces," ACS Nano **14**, 15042 (2020).
51. F. Callewaert, V. Velev, P. Kumar, *et al.*, "Inverse-designed broadband all-dielectric electromagnetic metadevices," Sci. Rep. **8**, 1358 (2018).
52. D. Sell, J. Yang, S. Doshay, *et al.*, "Large-angle, multifunctional metagratings based on freeform multimode geometries," Nano Lett. **17**, 3752 (2017).
53. J. Andkjær, V. E. Johansen, K. S. Friis, *et al.*, "Inverse design of nanostructured surfaces for color effects," J. Opt. Soc. Am. B **31**, 164 (2014).
54. B. Shen, P. Wang, R. Polson, *et al.*, "Ultra-high-efficiency metamaterial polarizer," Optica **1**, 356 (2014).
55. V. Neder, Y. Ra'di, A. Alù, *et al.*, "Combined metagratings for efficient broad-angle scattering metasurface," ACS Photonics **6**, 1010 (2019).
56. Y. Bao, L. Wen, Q. Chen, *et al.*, "Toward the capacity limit of 2D planar Jones matrix with a single-layer metasurface," Sci. Adv. **7**, eabh0365 (2021).
57. Y. Bao, F. Nan, J. Yan, *et al.*, "Observation of full-parameter Jones matrix in bilayer metasurface," Nat. Commun. **13**, 7550 (2022).
58. Z. Shi, A. Y. Zhu, Z. Li, *et al.*, "Continuous angle-tunable birefringence with freeform metasurfaces for arbitrary polarization conversion," Sci. Adv. **6**, eaba3367 (2020).
59. J. K. Gansel, M. Thiel, M. S. Rill, *et al.*, "Gold helix photonic metamaterial as broadband circular polarizer," Science **325**, 1513 (2009).
60. A. Basiri, X. Chen, J. Bai, *et al.*, "Nature-inspired chiral metasurfaces for circular polarization detection and full-Stokes polarimetric measurements," Light Sci. Appl. **8**, 78 (2019).
61. J. Hu, X. Zhao, Y. Lin, *et al.*, "All-dielectric metasurface circular dichroism waveplate," Sci. Rep. **7**, 41893 (2017).
62. M. Mutlu, A. E. Akosman, and E. Ozbay, "Broadband circular polarizer based on high-contrast gratings," Opt. Lett. **37**, 2094 (2012).